A Wireless-Implantable Microsystem for Continuous Blood Glucose Monitoring

Mohammad Mahdi Ahmadi, *Member, IEEE*, and Graham A. Jullien, *Life Fellow, IEEE*

***Abstract*—A remotely powered implantable microsystem for continuous blood glucose monitoring is presented. The microsystem consists of a microfabricated glucose biosensor flip-chip bonded to a transponder chip. The transponder chip is inductively powered by an external reader with a 13.56-MHz carrier. It then measures the output signal of the glucose biosensor and transmits the measured data back to the external reader using load-shift keying (LSK). The microsystem has a volume of 32 mm^3. The procedures for the microfabrication of the glucose sensor and the assembly of the microsystem are described along with the description of the circuit blocks of the transponder chip. The transponder chip has been fabricated with the TSMC 0.18-μm CMOS process and has a total area of 1.3 $\times$ 1.3 mm^2. The chip can measure the sensor output current ranging from 1 nA to 1 μA with less than 0.3% nonlinearity error, provided that the amplitude of the received RF signal is higher than 2.6 V; the circuit consumes a total current of about 110 μA.**

***Index Terms*—Amperometric sensor, glucose, implantable, implantable microsystem, microsystem, potentiostat, telemetry, transponder chip, wireless.**

I. Introduction

CONTINUOUS blood glucose monitoring can help to significantly reduce (between 40% to 75%) the symptoms associated with diabetes [1]–[3]. Currently, a few continuous blood glucose monitoring systems are commercially available which can continuously monitor the blood glucose level up to only a few days [4], [5]. A very promising approach to long-term continuous glucose monitoring is to implant a glucose sensor along with an electronic instrument, required for data measurement and communication, in the human body and measure the glucose level continuously. The sensor can be implanted just underneath the skin and be in contact with capillary blood or even interstitial fluid [6].

Most of the published works [7]–[15] that have employed the aforementioned idea suffer from some problems. First, the previously presented implantable units have relatively large sizes primarily due to the construction of the implantable device using discrete electronic components assembled on medium-size circuit boards; and second, due to using a battery for powering the implant. The size of the implant plays a key role in the success of the monitoring system [14]. A smaller implant can be more easily packaged and be simply implanted via outpatient surgery. It also provides more comfort for the patient and more options for the implantation site. However, the most important advantage of a smaller implant is that it promises a longer consistent in-vivo monitoring lifetime because a smaller implant is less sensitive to a patient's movement; thus, the tissue surrounding the implant comes to stability more rapidly and stays stable for a longer period of time [14].

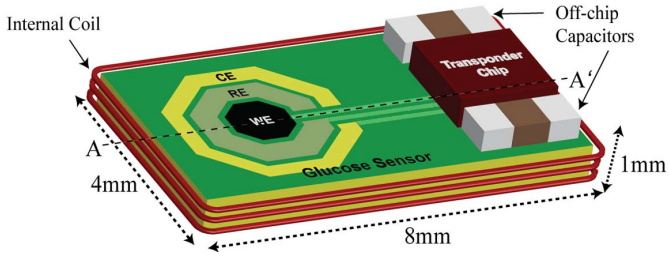

Fig. 1. Conceptual design of the proposed microsystem for continuous blood glucose monitoring.

A second problem of the previously published implantable units is that they have used conventional electrochemical glucose sensors (either oxygen-based or hydrogen peroxide-based sensors) for glucose sensing. The conventional sensors have several limitations when they are implanted in the body, such as the requirement for oxygen, short lifetime (low chemical stability), and interference from other chemical species, such as urate, ascorbic acid, and acetaminophen [16].

A third problem is associated with the requirement for batteries that can power the implant for a long period of time; not only does this result in an enlarged size of the implant but also decreases the lifetime of the implant.

Our approach to the aforementioned problems is to miniaturize the implantable unit by: 1) microfabricating the glucose sensor; 2) integrating all of the interfacing circuits into an integrated-circuit (IC) chip (transponder chip); and 3) attaching the microfabricated glucose sensor to the transponder chip using flip-chip bonding. Fig. 1 shows a conceptual design of our proposed microsystem.

Our glucose sensor is a novel electrochemical glucose biosensor developed at the research group of Prof. V. Birss in the Department of Chemistry at the University of Calgary [17], [18]. The sensor can function without the need for oxygen,

Manuscript received August 10, 2008; revised January 18, 2009. Current version published May 22, 2009. This work was supported in part by iCORE (Alberta), in part by Micronet R&D, and by NSERC. Personal use of this material is permitted. However, permission to use this material for any other purposes must be obtained from the IEEE by sending an e-mail to pubs-permissions@ieee.org. This paper was recommended by Associate Editor P. Mohseni.

M. M. Ahmadi was with the Department of Electrical and Computer Engineeering, University of Calgary, Calgery, AB T2N 1N4, Camada. He is now with Sound Design Technologies Ltd., Burlington, ON L7L 5P5 (e-mail: mmahmadi@ieee.org).

G. A. Jullien is with the Department of Electrical and Computer Engineering, University of Calgary, Calgary, AB T2N 1N4, Canada (e-mail: jullien@atips.ca).

Color versions of one or more of the figures in this paper are available online at http://ieeexplore.ieee.org.

Digital Object Identifier 10.1109/TBCAS.2009.2016844

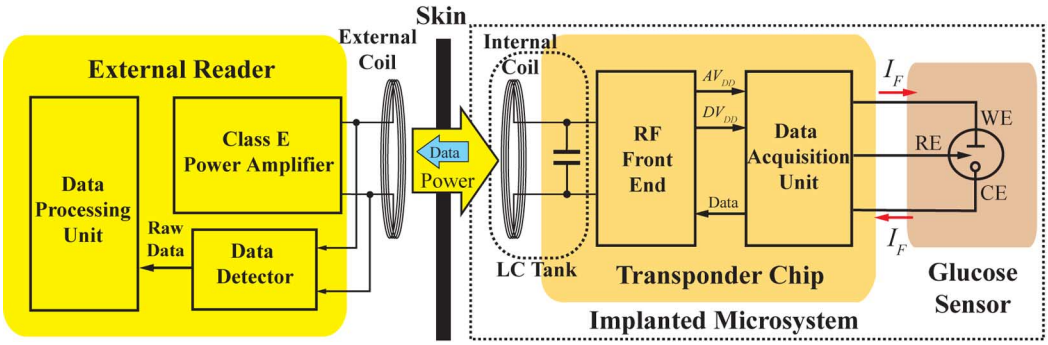

Fig. 2. Block diagram of the monitoring system.

and demonstrates good chemical stability, reproducibility, and biocompatibility [17], [18]. These characteristics make the sensor an appropriate choice for our microsystem.

Due to the problems associated with using a battery or a wired link [19], we have used a passive telemetry link for power and data transfer between the implantable microsystem and the external reader. The link operates at the industrial-scientific-medical (ISM) frequency band of 13.56 MHz.

This paper describes the general aspects of the microsystem with more concentration on the transponder chip and its characterization results. Section II provides a systematic overview of our monitoring system and its data transmission protocol. Section III describes the circuit details of the transponder chip. Section IV presents the procedures for the microfabrication of the glucose sensor and the hybrid integration of the microsystem. Section V briefly describes the external reader and Section VI presents experimental results. Section VII discusses some issues regarding the implantation of the microsystem in the body, and Section VIII concludes this paper.

II. Monitoring System Overview

Fig. 2 shows a simplified block diagram of the monitoring system consisting of an implantable microsystem and an external reader. The external reader generates a high-frequency magnetic field in an external coil (primary coil), through which power is inductively transferred to an internal coil (secondary coil) which is connected to the implantable microsystem. The microsystem measures the blood glucose concentration and transmits the measured data to the external reader by using load-shift keying (backscatter modulation).

The required data-transmission rate for continuous blood glucose monitoring is very low. One measurement with 5% accuracy [11] every 10 min [20] can adequately describe the dynamics of blood glucose variation. As a result, our proposed strategy is to turn on the external reader every 10 min through which the microsystem is powered. The microsystem is kept on for about 2 min in order for the glucose sensor to settle to its final value.

The glucose sensor used in our microsystem is an amperometric electrochemical biosensor which generates a current proportional to the glucose concentration. It consists of three electrodes: 1) a working electrode (WE); 2) a reference electrode (RE); and a counter electrode (CE).

The working electrode serves as a surface on which the electrochemical reaction takes place between the glucose and an enzymatic layer coated over the electrode. The enzymatic layer contains glucose oxidase which is an enzyme, specific to glucose. It catalyzes the oxidation of glucose to gluconic acid, producing a small electric current at the electrode. The new glucose sensor employed in our microsystem uses iridium–oxide nanoparticles to mediate the transfer of the electrons from the reduced enzyme to the working electrode. This approach eliminates the need for oxygen (which has low concentrations in the body) and extends the lifetime of the glucose sensor since it does not produce hydrogen peroxide (which plays a major role in reducing the lifetime of the glucose sensor).

The reference electrode is used to measure the solution (blood or interstitial fluid) potential. The counter electrode is an inert conductor (gold) that supplies the current required for the electrochemical reaction taking place at the working electrode.

The transponder chip consists of two main blocks: 1) an RF front-end block and 2) a data-acquisition (DAQ) unit. The RF front-end block receives the RF signal that is induced in the internal coil, rectifies it, and generates the supply voltage required for the operation of the DAQ unit. It also comprises a load modulation circuit, which modulates the current dissipated in the implant according to the received data from the DAQ unit.

A very simple protocol for data transmission was developed which enables us to transmit the glucose concentration data with minimum on-chip circuit blocks and very low power consumption. The DAQ unit converts the sensor current I_F to a pulse waveform, for which the time difference between two consecutive pulses T is inversely proportional to the sensor current as

$$T = \frac{K}{I_F} \tag{1}$$

where K is the proportionality constant. The pulsewidth of the waveform, defined by D, is constant and known.

As shown in Fig. 3, the envelope of the received RF signal on the internal coil changes according to the load modulation in the transponder chip. Subsequently, due to the coupling between the external and internal coils, the envelope of the transmitted RF signal changes too. The external data detector senses these envelope fluctuations and generates another pulse waveform. Due to the low-pass filtering nature of the power transfer link, the pulsewidth of the externally reconstructed waveform, shown by D_{ext}, is larger than D and is also signal dependent.

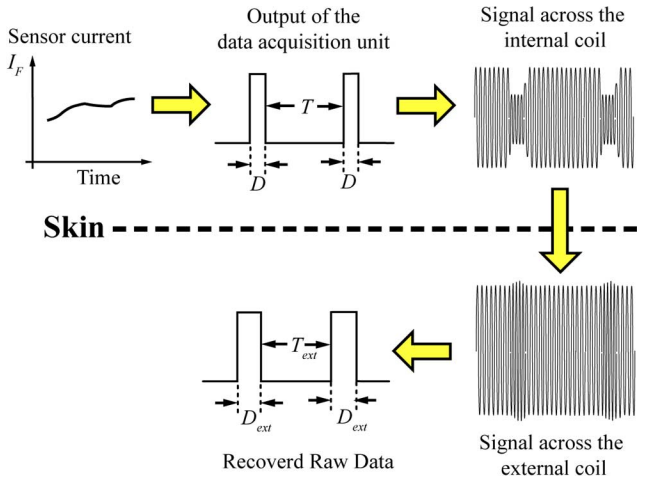

Fig. 3. Data measurement and transmission strategy.

Thus, in order to recover the data, the frequency of the external pulse waveform f_{data} is measured (which is exactly equal to the frequency of the internal pulse) and since D is constant and known, I_F is recovered by using

$$I_F = \frac{K}{\left(f_{\text{data}}^{-1} - D\right)}. \tag{2}$$

III. Transponder Chip

The transponder chip was fabricated by using TSMC's 0.18-μm CMOS process. All of the circuit blocks in the RF front end, excluding the bandgap bias circuit, were designed by using 3.3-V transistors which have 7-nm-thick gate oxides. The DAQ block was designed with 1.8-V transistors which have 4-nm-thick gate oxide.

The chip occupies an area of 1.3×1.3 mm^2. The chip area is limited by the required number of pads for test purposes. The main core circuit occupies an area of about 0.2 mm^2. The unused active area was filled with capacitors required for the analog and digital supplies and also for a resonance capacitor C_S, resonating with the internal coil at 13.56 MHz. Fig. 14(a) shows a microphotograph of the transponder chip.

A. RF Front End

Fig. 4 shows the block diagram of the RF front end. The first blocks connected to the internal coil are two RF limiters which clamp the amplitude of the induced RF signal in order to avoid electrical overstress on the gates and pn junctions of the core transistors.

The voltage rectifier block rectifies the received RF signal and charges up an off-chip storage capacitor C_{DH} to an unregulated dc supply voltage. The following block, the load modulator, is responsible for changing the load current of the rectifier, and finally, a voltage regulator produces two regulated dc supply voltages: one for the analog circuit blocks AV_{DD} and one for the digital circuits DV_{DD}. The reference voltage for the voltage regulator is generated by a current-mode bandgap bias circuit [21].

An important parameter of the voltage regulator is its power-supply ripple rejection ratio (PSRR). The input voltage to the regulator V_{DH} is an unregulated dc voltage, while its output is a clean dc voltage. As a result, to improve the PSRR of the circuit, the supply voltage of the bias circuit is obtained from the output of the regulator. This strategy makes use of a power-on-reset (PoR) circuit necessary in order to drive the circuit from its zero condition during startup. Thus, a closed-loop power-on-reset circuit is designed to force the voltage regulator out of the zero quiescent state.

1) RF Limiter: Minimizing the power consumption of the transponder chip is very important because: first, the available power to a biomedical implant is limited; second, because it increases the read range of the transponder chip; and third, it minimizes the risk of the damage to the surrounding tissue due to any temperature increase in the transponder chip.

An obvious approach to minimizing the power consumption and improving the performance of a circuit is to design the circuit using more advanced IC fabrication technologies. However, the oxide and junction breakdown voltages in these technologies are limited to only a few volts. Since it is extremely difficult to keep the external and internal coils in a constant position, the distance between these coils may decrease, resulting in stronger induced RF signals in the internal coil (possibly up to tens of volts). As a result, two RF limiter blocks are required to clamp the amplitude of the induced RF signal.

Fig. 5 shows the circuit schematic of the RF limiter. When the RF voltage exceeds the sum of the threshold voltages of M_1 and M_2, a current starts to flow in R_1 which, in turn, gradually turns M_3 on. When the voltage across R_2 exceeds the threshold voltage of M_4, M_4 turns on and draws a considerable amount of current from $RF1/RF2$, which, in turn, reduces the amplitude of the received RF signal. RF limiters were designed to clamp the amplitude of the RF signal at 3.3 V.

2) Voltage Rectifier: Using a half-wave rectifier slightly simplifies the design of the RF front end. However, the reverse voltage stress on the rectifying diodes is larger in a half-wave rectifier than that in a full-wave bridge rectifier. Thus, we designed a full-wave rectifier with a schematic shown in Fig. 6.

M_3 and M_4 operate as switches to minimize the voltage drop between the substrate (ground) of the chip and $RF1/RF2$. M_1 and M_2 are diode-connected and their bulk terminals are connected to their drain terminals, resulting in a lower voltage drop across M_1 and M_2. This reduced voltage drop is due to the following two reasons.

First, since the source-to-bulk voltage V_{SB} of M_1 and M_2 is positive when either passes the current, because of body effect, the threshold voltage of those transistors is reduced to a value less than its nominal value.

Second, the parasitic p^+/n-well diodes of the source terminals of the transistors (i.e., D_1 and D_2), work in parallel with M_1 and M_2.

The reduction in the voltage drop across the rectifier is important because it reduces the dissipated power in the rectifier, which is a major source of power dissipation in the chip. In addition, it enables the chip to be powered with weaker received RF signals.

If, because of high current, the voltage drop across M_3 and M_4 increases, the parasitic p–sub/n^+ diodes of M_3 and M_4, as shown in Fig. 6, turn on and help to minimize the voltage drop.

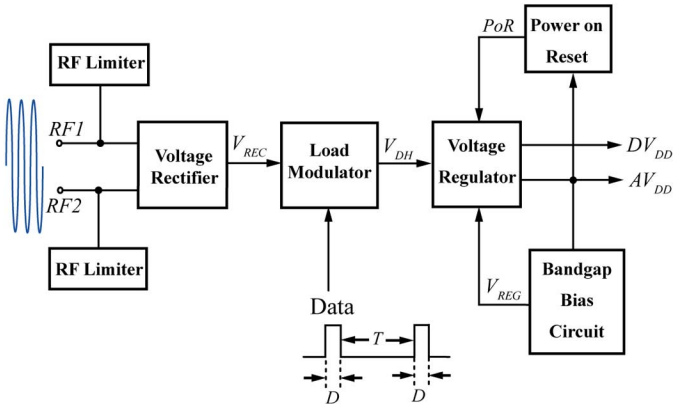

Fig. 4. Block diagram of the RF front end.

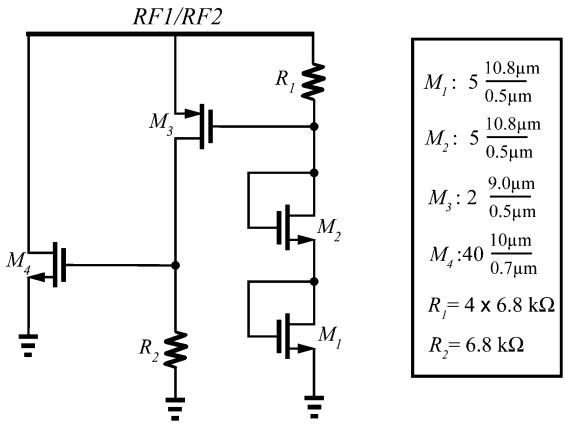

Fig. 5. RF limiter.

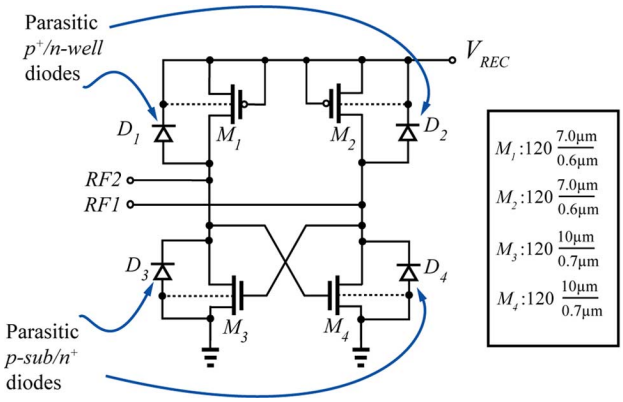

Fig. 6. Voltage rectifier.

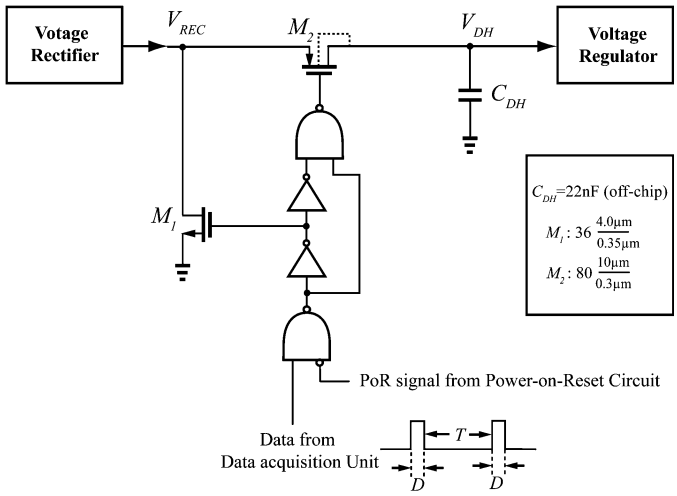

Fig. 7. Load modulator.

Since the bulk terminals of M_1 and M_2 are not always connected to the highest voltage in the chip, there is a risk of latch-up in the rectifier [22]; thus, very wide n^+ guard rings were placed around M_1 and M_2, and very wide p^+ guard rings were placed around M_3 and M_4 to minimize the risk of latch-up.

The aspect ratio of transistors M_3 and M_4 are very large because they should be able to pass not only the current flowing through M_1 and M_2, but also the large currents that are sunk by the RF limiters.

Based on the measurement results, the voltage drop across the voltage rectifier is about 0.57 V for a loading current of 110 μA with a 22-nF storage capacitor. This voltage drop is relatively low, considering that the nominal threshold voltage of 3.3-V PMOS transistors in the process is higher than 0.7 V.

The series resistance of the interconnect traces between the rectifier and the pads connected to the internal coil and the storage capacitor must be kept as low as possible because large currents flow in these traces and a series resistance as small as 3 Ω can reduce the read range by several centimeters [23]. Therefore, multiple layers of wide metal lines were used for these traces.

3) Load Modulator: Fig. 7 shows the load modulation circuit. The circuit turns M_1 on when the output pulse of the DAQ unit is high (during the time period of D) and turns it off when the signal is low (during the time period of T); when M_1 is on, it sinks a considerable amount of current from the output of the rectifier $V_{\rm REC}$, creating a large load for the internal coil. At the same time, M_2 is off to prevent discharging the storage capacitor $C_{\rm DH}$ to the ground.

To simplify the data detection in the external reader, M_1 should have enough strength to create more than 30% modulation depth on the envelope of the signal across the internal coil.

A logic circuit is placed before the gate of M_1 and M_2; first, to block data transmission during the startup of the chip (when the power-on-reset circuit is active), and second, to create a nonoverlapping logic signal for switching M_1 and M_2 (otherwise, M_1 and M_2 might be simultaneously on, discharging $C_{\rm DH}$ to ground).

From the previous discussion, we note that during the time period T, (in which M_1 is off and M_2 on), the full-wave rectifier charges up $C_{\rm DH}$, while during the time period D, the power for the chip is supplied from the stored charge in $C_{\rm DH}$. Thus, D should be short enough to prevent discharging of $C_{\rm DH}$ below the minimum required supply voltage for the voltage regulator. But on the other hand, too short a period for D results in very sharp load changes that cannot be detected by the external reader. In this work, D was chosen to be about 2.5 μs as a compromise between the aforementioned tradeoffs.

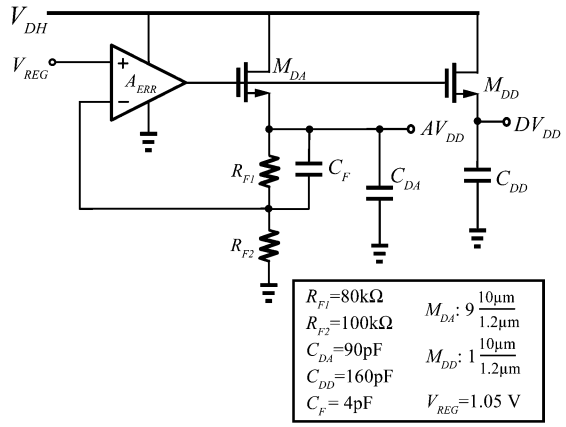

Fig. 8. New voltage regulator generating two isolated outputs.

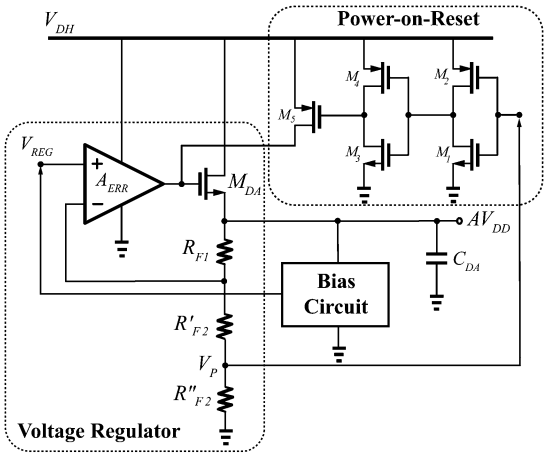

Fig. 9. Power-on-reset circuit.

4) Voltage Regulator: The voltage regulator is one of the most important circuit blocks in remotely powered systems. The regulator should produce a clean and stable supply voltage, while consuming very low power and having a very low voltage dropout.

A major problem in radio-frequency identification (RFID) and medical implant applications (and, generally, in most mixed-signal circuits) is the supply noise due to fast switching in the digital circuitry [23]. The conventional solution to block the digital supply noise from being injected into the analog supply is to use two voltage regulators: one for the analog circuits and the other for the digital circuits. Clearly, the power required for the voltage regulation is almost double using this approach.

Fig. 8 shows our proposed voltage regulator structure which isolates $AV_{\rm DD}$ from $DV_{\rm DD}$, without adding any extra power consumption, chip area, or even complexity to the circuit. A linear series voltage regulator is used to generate $AV_{\rm DD}$. To protect $AV_{\rm DD}$ from the switching noise in $DV_{\rm DD}$, the pass transistor of the regulator is divided into two transistors; M_{DA} generates $AV_{\rm DD}$ in the closed-loop feedback of the voltage regulator, while $M_{\rm DD}$ generates $DV_{\rm DD}$ in an open-loop circuit. Due to the closed-loop control, $AV_{\rm DD}$ is very well defined at 1.8 V; but because $DV_{\rm DD}$ is not generated with a feedback circuit, it is not very well controlled; however, this is not important as it generates the supply voltage for the digital circuits. As a consequence of the aforementioned approach, $AV_{\rm DD}$ and $DV_{\rm DD}$ are well isolated and measurements of the circuit show more than 40 dB of isolation between them.

In order to achieve low dropout voltage regulation, M_{DA} and $M_{\rm DD}$ are realized with native (zero-threshold) MOS transistors. C_F is added in order to create a left-half-plane zero in the feedback loop and, thus, improve the stability of the regulator.

The current consumption of the regulator is 22 μA. The circuit shows a line regulation of 30 mV/V, a ripple rejection of 28 dB (at 13.56 MHz), and a dropout voltage of 120 mV for $AV_{\rm DD}$ and $DV_{\rm DD}$ outputs. The load regulation for $AV_{\rm DD}$ is 18 mV/mA and for $DV_{\rm DD}$, it is 450 mV/mA.

5) Power-on-Reset: The design of a power-on-reset circuit that works reliably at all of the process, temperature, and supply voltage corners and with any load condition is quite challenging. Fig. 9 shows the schematic of our proposed power-on-reset circuit. When $AV_{\rm DD}$ is zero, V_P is zero; thus, M_5 connects the gate of M_{DA} to V_{DH}, which results in powering up the regulator output $AV_{\rm DD}$. When V_P is high enough, M_5 turns off and $AV_{\rm DD}$ is controlled by the feedback loop of the regulator.

In order for the circuit to work properly, the W/L ratio of M_2 should be chosen to be very small (e.g., 1/10) and the W/L ratio of M_1 should be very high (e.g., 10/1). Under these conditions, the switching threshold voltage of the M_1-M_2 inverter is almost equal to the transistor threshold voltage of M_1, defined by V_{tn}.

In order for the power-on-reset circuit to switch to its off state at a proper time, the value of resistor R'_{F2} and R''_{F2} should be chosen based on the following inequality:

$$\frac{V_{tn,\max}}{AV_{\rm DD,des}} < \frac{R''_{F2}}{R_{F1}+R'_{F2}+R''_{F2}} < \frac{V_{tn,\min}}{AV_{\rm DD,min}} \qquad (3)$$

where $V_{tn,\max}$ and $V_{tn,\min}$ represent the upper and lower levels of V_{tn} with respect to process and temperature variations; $AV_{\rm DD,min}$ represents the minimum supply voltage under which the bandgap bias circuit outputs the desired reference voltage for the regulator. $AV_{\rm DD,des}$ represents the desired output voltage of the regulator (in this case, 1.8 V).

Based on (3), it is important to design the bias circuit such that it can function properly with a supply voltage as low as $(V_{tn,\min}/V_{tn,\max})AV_{\rm DD,des}$.

B. DAQ Unit

Fig. 10 shows the block diagram of the DAQ unit which consists of an electronic potentiostat, a current-to-frequency (I-to–F) converter, and the bandgap bias circuit which is common between the RF front end and the DAQ unit.

The potentiostat interfaces with the glucose sensor and generates a mirrored image I_{F1} of the sensor current I_F. I_{F1} is then injected into a I-to-F converter, which generates a pulse waveform, for which the time difference between two consecutive pulses is inversely proportional to I_F.

In order to prevent injection of the switching noise from the I-to-F converter into the sensitive analog circuits, an independent bias circuit was designed for the I-to-F converter.

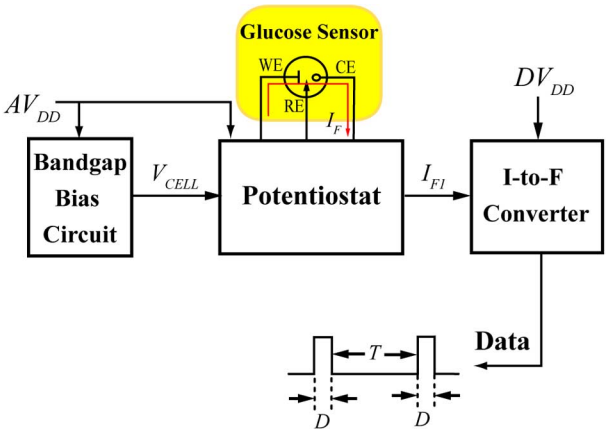

Fig. 10. Block diagram of the DAQ unit.

1) Potentiostat: A potentiostat is an electronic instrument that controls the voltage difference between the working and reference electrodes of an electrochemical cell by sinking or sourcing a current from or into the electrochemical cell through the counter electrode. In almost all applications, the potentiostat measures the current flowing between the working and the counter electrodes.

While state-of-the-art potentiostats are now integrated in complementary metal–oxide semiconductor (CMOS) technologies [23]–[32], there is still a demand for very low power circuits required for remotely powered biomedical implants. Fig. 11 illustrates the structure of our proposed potentiostat [33]. Since our glucose sensor generates oxidation current (the direction of the sensor current is from the working electrode to the counter electrode), in order to increase the headroom for the signal swing at the counter electrode, the working electrode is directly connected to $AV_{\rm DD}$. A_1 and M_1, together, control the voltage difference between the working and the reference electrodes by sinking current from the counter electrode. At the same time, M_2 generates a mirrored image of I_F. The mirrored current I_{F1} is then injected into the I-to-F converter.

The cell potential $V_{\rm CELL}$ is applied between $AV_{\rm DD}$ and the inverting input of A_1. The direct connection of the working electrode to $AV_{\rm DD}$, which is an ac ground, reduces the noise and interference pickup at the working electrode and improves the stability of the potentiostat [33].

To minimize the kickback effect from the I-to-F converter to the potentiostat, I_{F1} is mirrored again before being delivered to the I-to-F converter. A cascode structure is used to realize the current mirrors M_1-M_2 and M_3-M_4 to improve mirror matching. The potentiostat consumes a total current of 18 μA.

2) I-to-F Converter: Fig. 12 shows the circuit schematic of the I-to-F converter [34]. The operation of the circuit can be seen by assuming that the output of the flip-flop is off (i.e., M_5 is on and M_6 is off). Therefore, the mirrored current of the sensor I_{F2} is integrated in $C_{\rm INT}$ until the voltage across $C_{\rm INT}$ and $V_{\rm INT}$ exceeds V_{R1}. Then *Comp1* sets the flip-flop where a reference current $I_{\rm REF}$ starts to discharge $C_{\rm INT}$ until $V_{\rm INT}$ reaches V_{R2}. Finally, *Comp2* resets the flip-flop, and this cycle repeats. Thus, $V_{\rm INT}$ is a sawtooth waveform, and the output of the flip-flop is the desired data waveform.

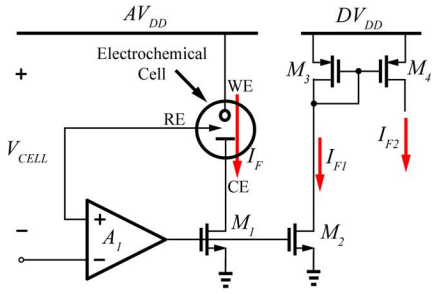

Fig. 11. Potentiostat.

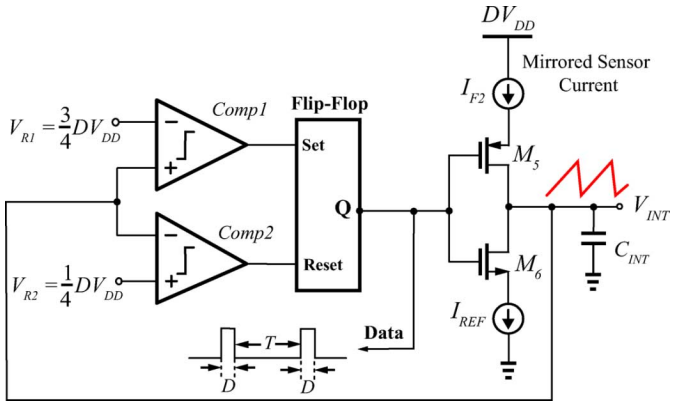

Fig. 12. Current-to-frequency converter.

The time difference between two consecutive pulses T can be expressed as

$$T = \frac{DV_{\rm DD}C_{\rm INT}}{2I_{F2}} \tag{4}$$

and the pulse width D is

$$D = \frac{DV_{\rm DD}C_{\rm INT}}{2I_{\rm REF}}. \tag{5}$$

Thus, T is inversely proportional to the mirrored current of the sensor I_{F2} and D is constant. Since $I_{\rm REF}$ is chosen to be larger than the maximum value of the sensor current, D will be always shorter than T. The proportionality constant K, defined in (1), can then be derived from (4) to be

$$K = \frac{DV_{\rm DD}C_{\rm INT}}{2}. \tag{6}$$

Since $C_{\rm INT}$ and $I_{\rm REF}$ are subject to process variations, K and D are process-dependent; thus the transponder chip will be required to be calibrated before implantation by measuring $I_{\rm REF}$ and D, where K is determined by using (5) and (6).

V_{R1} and V_{R2} are generated by a voltage divider, realized by diode-connected PMOS transistors to save power and chip area. The I-to-F converter consumes a total current of 10 μA.

IV. Sensor Fabrication and Microsystem Assembly

The new glucose sensor used in our microsystem is an amperometric biosensor, functioning based on the three-electrode electrochemical measurement system. The details of the original construction of the sensor and the experiments performed on the sensor are described in [17] and [18].

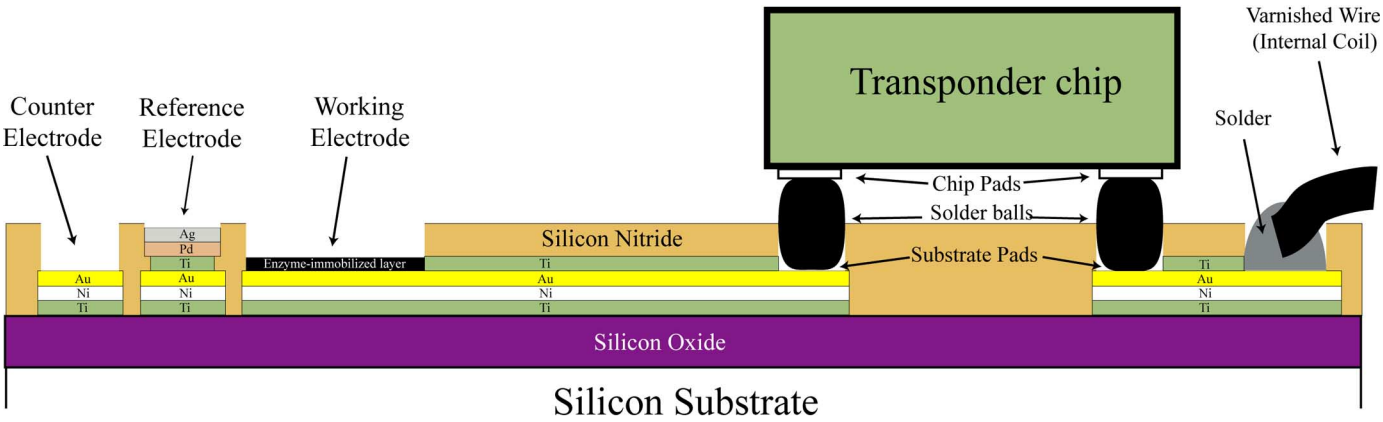

Fig. 13. Cross-sectional view (A-A′) of the microsystem illustrated in Fig. 1.

The working electrode of the sensor plays the principal role in glucose sensing. It is constructed by immobilizing an enzymatic layer over a gold electrode using a sol-gel approach. The sol-gel solution is a mixture of glucose oxidase, Nafion and iridium nanoparticles suspended in a mixed solvent of ethanol and water. The counter electrode of the sensor is also built of another gold electrode and the reference electrode is a pseudo (quasi) Ag/AgCl electrode [35], [36].

The gold electrodes required for the working and counter electrodes were created by depositing and patterning a stacked metal of titanium-nickel-gold (40 nm-400 nm-400 nm). The metallization was also utilized for interconnect metal traces and bonding pads.

The titanium layers act as adhesion promoter between the metallization and the sensor substrate. The nickel layer primarily acts as a diffusion barrier layer preventing the corrosion of the adhesion layer by creating a barrier against the metal species and ionic contaminants which may diffuse from the top metal layers or from the solder bump into the adhesion layer [37].

Usually, a thickness of a few tens of nanometer of nickel is enough to act as a diffusion barrier layer [37], but we increased the thickness of the nickel layer to about 400 nm in order to partially use it as a solder-wettable layer required for the bonding pads. The final gold layer acts as the counter and working electrode for the glucose sensor. It also acts as an antioxidation layer required for the bonding pads. We increased the thickness of gold to about 400 nm in order to partially use it as the solder-wettable layer in addition to the nickel layer.

For the reference electrode metallization, titanium-palladium-silver (50 nm-50 nm-600 nm) metallization was selected because of its excellent corrosion characteristics [35].

Fig. 13 illustrates the cross-sectional view (A-A′) of the microsystem shown in Fig. 1. The procedure for the microfabrication of the glucose sensor is as follows. A 4-in silicon wafer coated with a 500-nm silicone oxide layer was used as the substrate for the sensor and the microsystem. The oxide layer provides the insulation between sensor electrodes.

Then, the titanium-nickel-gold-titanium metallization required for the working electrode, counter electrode, interconnect traces, and bonding pads was deposited and patterned over the substrate using a lift-off process. The top titanium layer works as an adhesion layer between the metallization and the passivation layer deposited over the metallization.

Next, a plasma-enhanced chemical vapor deposition (PECVD) process was used to deposit an 800-nm silicon nitride passivation layer over the wafer. Silicon nitride was chosen as the passivation layer because it is less permeable to water vapor and alkali ions rather than silicon oxide. A reactive ion etching (RIE) process is then used to etch away the silicon nitride from the active areas, such as sensor electrodes and bonding pads. Next, the top titanium layer of the deposited metallization was removed in the active areas by immersing the wafer in a titanium etchant (a 5% hydrogen fluoride solution).

Next, the titanium-palladium-silver metallization required for the reference electrode was deposited and patterned by using a second lift-off process.

The next step in fabricating the glucose sensor is to deposit the enzymatic solution over the working electrode; but because the glucose oxidase contained in the enzymatic solution denatures above 65 °C [38], this step needs to be performed at low temperatures without any high-temperature postprocessing. Since, in a flip-chip bonding process, the temperature of the substrate and the chip has to be raised up to the melting point of the solder bumps (which is above 200 °C), the enzyme-immobilization process should be performed after flip-chip bonding.

The wafer was then diced to individual substrates and then a transponder chip was flip-chip bonded to one of the microsystem substrates using a Karl–Suss FC150 flip-chip bonder. The bonding pads of the transponder chip were bumped with indium-lead solder balls before the flip-chip bonding process. The solder-bumping process was performed on singulated dies by a vendor (CVInc). Then, the off-chip components, including two capacitors and the internal coil inductor, were connected to the substrate by using either solder paste (a conductive epoxy can also be used). The internal inductor was a five-turn rectangular coil (4 mm × 8 mm) made of varnished wire (AWG 38) wound around the perimeter of the microsystem.

A 2-mm-thick poly-dimethylsiloxane (PDMS) hard mask with a 1-mm circular opening was created by using a stainless-steel mold and then placed over the sensor substrate such that the circular opening was over the working electrode. Next, a very small droplet of the enzymatic mixture was poured into the opening of the PDMS mask using a micropipette. The

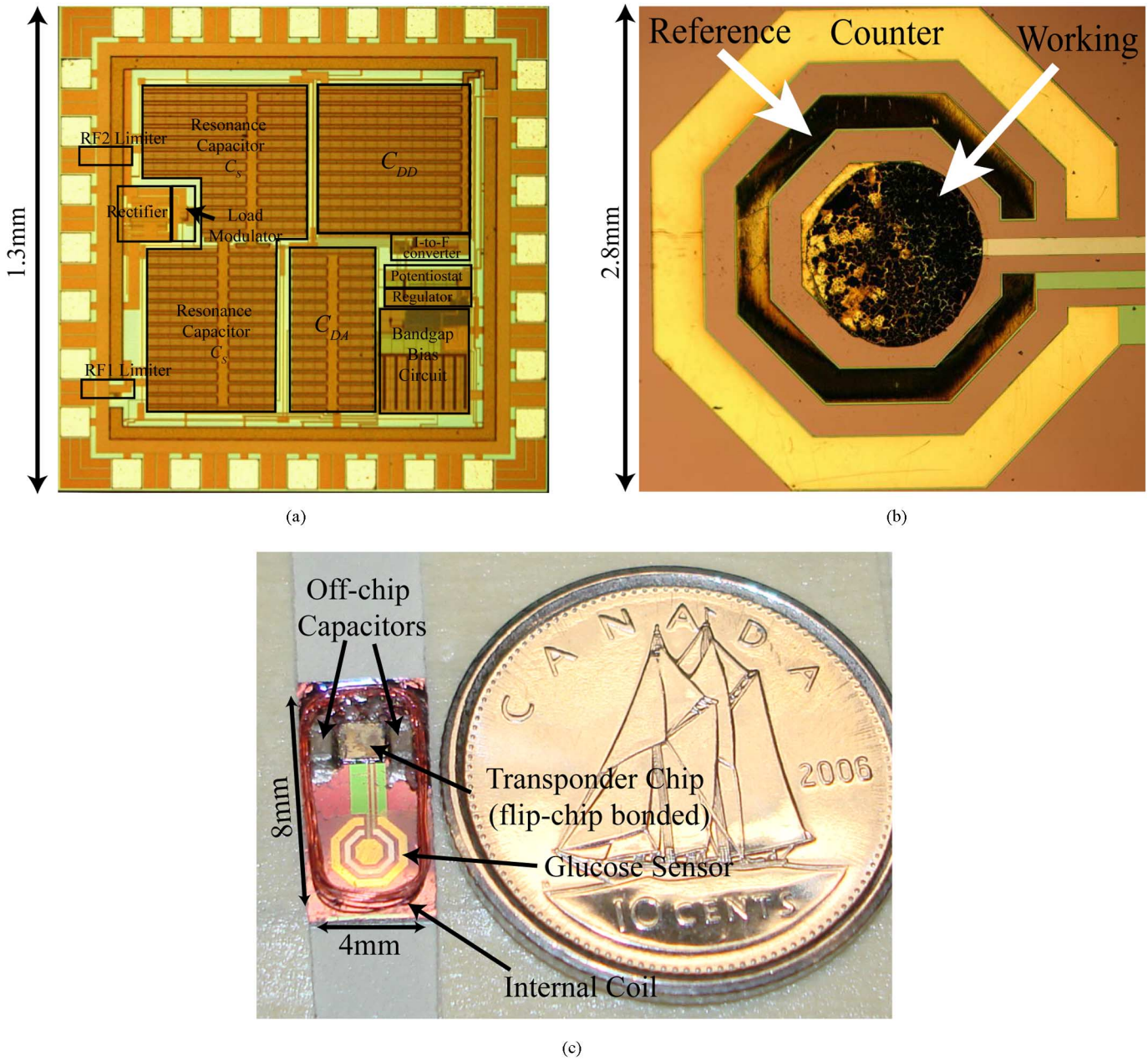

Fig. 14. (a) Microphotograph of the transponder chip. (b) Microphotograph of the glucose sensor. (c) Photograph of one of the assembled microsystems (before packaging and enzyme immobilization) next to a dime.

mixture was left to dry for a few minutes and, finally, the PDMS mask was removed. Fig. 14(b) shows a microphotograph of the glucose sensor after enzyme immobilization and Fig. 14(c) shows a photograph of one of the assembled microsystems.

Part of the rationale behind using PDMS as a hard mask is that PDMS has dangling silanol bonds [39]. When the PDMS mask is attached to the sensor substrate, some molecular bonds are created between the PDMS and the top layer of the sensor substrate (silicon nitride), preventing the enzymatic mixture from leaching between the PDMS mask and the substrate. In addition, PDMS is an inert and nontoxic material, which does not react with the enzymatic mixture.

The next stage is the packaging of the microsystem which is necessary to protect the interconnection conductors and off-chip components from the blood and interstitial fluid, which are highly corrosive materials. Materials, such as epoxy, silicone, and Parylene C can well protect the microsystem for a few months [35] and have been previously used for the packaging of implantable devices [7], [8], [13] with satisfactory results.

For our in-vitro tests, we used MED6–6606 (Nusil Technology), which is a one-part silicone dispersion material, to package the microsystem. This silicone has a low viscosity and designed for dipping or wiping. As a result, packaging of the microsystem was performed very simply only by dipping those sides of the microsystem that had to be packaged into the silicone.

As a final remark, it should be noted that the performance of the reference electrode is very critical in an electrochemical

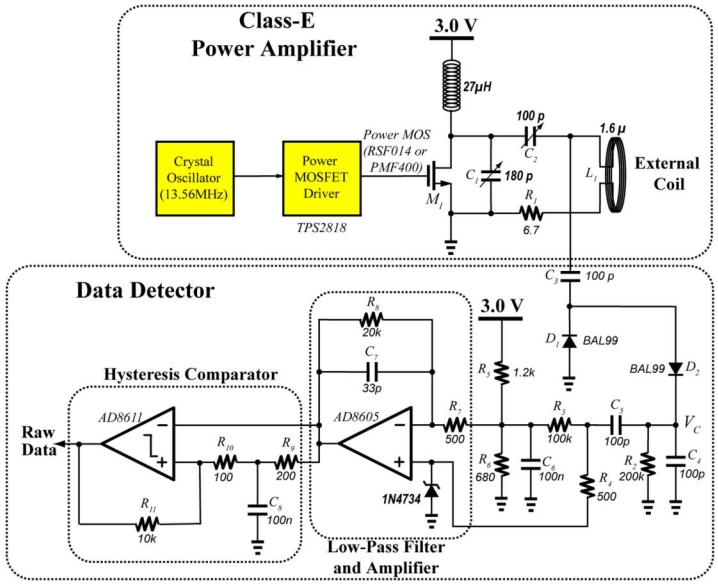

Fig. 15. Simplified schematic of the external reader.

experiment, as variations in the reference electrode potential directly shift the working electrode potential, which itself changes the redox current. A pseudo Ag/AgCl reference electrode [35], [36] can satisfactorily function if two conditions are met: 1) the chloride concentration of the test solution is relatively constant and 2) the current in the reference electrode is very small. Fortunately, both conditions are met for this work. First, the microfabricated glucose biosensor is intended to be used in blood, whose chloride concentration is almost constant (350–375 mg/dL or 98–106 mM), and second, because of using a three-electrode electrochemical sensor in this work, the current in the reference electrode is considerably small.

For our in-vitro experiments, we left the sensor in a phosphate buffer solution with NaCl (100 mM) (the solution we used for our experiments) for a few hours in order to convert the surface of the silver electrode to AgCl. We believe that in an in-vivo test, the conversion of the surface of the silver electrode to AgCl is accomplished during the first few hours after the implantation through the chloride ions contained in the blood.

More details about the microfabrication and the hybrid integration of the microsystem can be found in [40].

V. External Reader

Fig. 15 illustrates the circuit schematic of the external reader used in our experiments. A class-E power amplifier, operating at 13.56 MHz, was designed to generate the carrier that powers up the microsystem. L_1 functions as the external coil. It was realized with a four-turn circular spiral inductor with an outer diameter of 44 mm over a printed-circuit board (PCB).

The input of the data detector is extracted from the resonating node of the power amplifier (the node between L_1 and C_2) because the signal has a larger amplitude at this node. C_3 and D_1 shift the negative peak of the RF signal to zero. The level shifting also acts as a voltage doubler on the signal. D_2, R_2, and C_4 form an asynchronous envelope detector. Usually, the amplitude of the RF signal is in the order of tens of volts, thus the dc level of the signal at node V_C is at the same range. C_5 blocks the dc level of the signal and makes its processing convenient for the subsequent stages. R_7, R_8, C_7, and the amplifier AD8605 generate a low-pass filter with 32-dB gain in its passband. The low-pass filter amplifies the signal and rejects the ripples at the carrier frequency. Finally, a hysteresis comparator, composed of R_{9-11}, C_8, and the comparator AD8611, is used to digitize the signal.

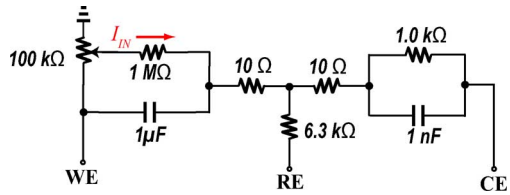

Fig. 16. Circuit, emulating the glucose sensor, used for calibrating the transponder chip.

VI. Experimental Results

Before characterizing the entire monitoring system, quantifying the precision and accuracy of the transponder chip and the telemetry link in measuring the sensor current and in transmitting the measured data to the external reader is required. In order to do that, a circuit emulating the electrical behavior of our glucose sensor was connected to the transponder chip, and the chip was powered through the telemetry link.

The circuit used for emulating the glucose sensor is shown in Fig. 16 [33]. The experiment was conducted as follows. The emulated sensor current I_{IN} was varied by using the 100-kΩ potentiometer and the average frequency of the received raw data at the external reader was measured by using a Tektronix TDS5054B digital oscilloscope. Using the measured frequency, the transmitted data I_{meas} was recovered by means of (2).

I_{IN} was swept from 1 nA to 1 μA (the current range of the actual glucose sensor is in the range of 10 nA to 300 nA, depending on the area of the sensor). Fig. 17 shows the oscilloscope waveforms of the critical nodes for I_{IN} of 400 nA. This experiment

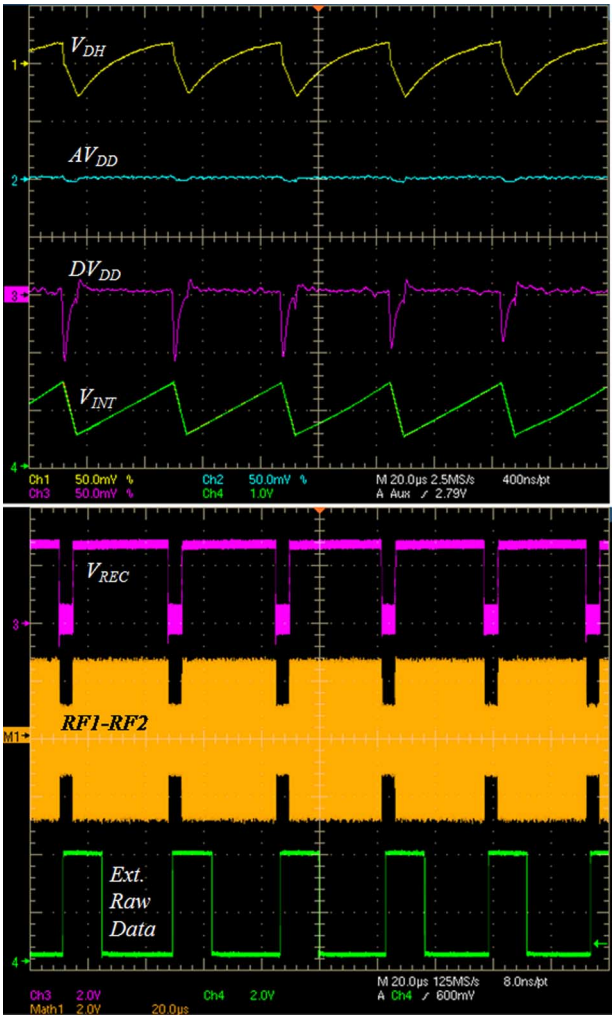

Fig. 17. Transient waveform of the critical nodes of the monitoring system for the input current of 400 nA; from top: $V_{\rm DH}$ (oscilloscope coupling: AC, 50 mV/div), $AV_{\rm DD}$ (oscilloscope coupling: AC, 50 mV/div), $DV_{\rm DD}$ (oscilloscope coupling: AC, 50 mV/div), $V_{\rm INT}$ (1.0 V/div), $V_{\rm REC}$ (2.0 V/div), signal across the internal coil RF1-RF2 (2.0 V/div), and the detected raw data by the external reader (2.0 V/div).

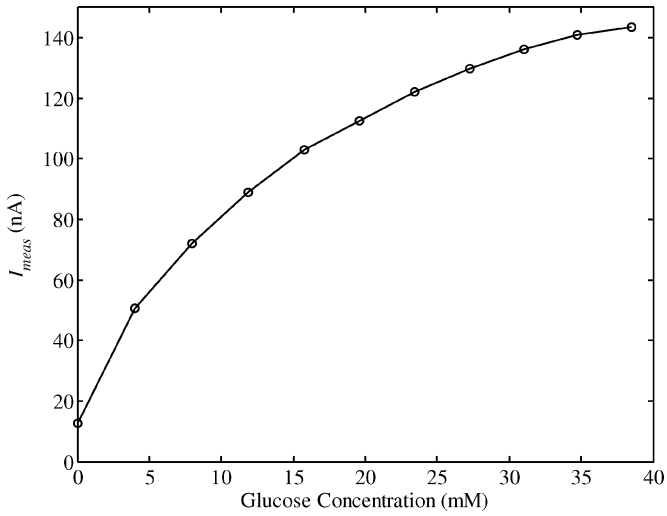

Fig. 18. Measured response of the overall monitoring system to the change in glucose concentration.

TABLE I
SUMMARY OF THE CHARACTERISTICS OF THE TRANSPONDER CHIP, TELEMETRY LINK , AND THE GLUCOSE SENSOR

Transponder Chip	
Die area	1.69 mm^2
Technology	0.18 μm CMOS
Full scale measurable current	1 μA
Minimum resolvable current	< 1 nA
Integral Nonlinearity Error	0.3 %
Current consumption	110μA
Supply Voltage	1.8 V
Telemetry Link	
Modulation Scheme	LSK
Read Range*	4 cm
Carrier Frequency	13.56 MHz
External coil	1.6 μH
Internal coil	500 nH
Glucose Sensor	
Area of WE	0.83 mm^2
Area of RE	1.0 mm^2
Area of CE	2.33 mm^2
Glucose Detection Range	0-40 mM
Cell Potential	0.6 V

*If the internal and external coils are properly tuned.

revealed that the telemetry system, including the transponder chip and the telemetry link and the data detection circuit, has less than 0.3% integral nonlinearity error (the maximum percentage error between the ideal output of the monitoring system and the measured output level).

In order to test the performance of the overall proposed monitoring system in measuring glucose concentration, a nonstirred aerated phosphate buffer solution (pH 7) with 100 mM NaCl was used. In the human body, the blood glucose concentration is normally in the range of 4 to 8 mM. This range for diabetic people is wider (i.e., 2 to 30 mM). Thus, in our experiment, we increased the glucose concentration of the solution from 0 to more than 30 mM, by gradually adding glucose to the solution. After settling the sensor current to its final value (in approximately 2 min), the transmitted data were measured by using the approach explained before. Fig. 18 shows the measured currents by the monitoring system for different glucose concentrations.

As is clear in Fig. 18, the response of the sensor is not very linear which is due to fact that we have not placed a diffusion limiting layer over the glucose sensor; thus, it was functioning in a mass-transport limited regime [36]. As is explained in Section VII, when the sensor is implanted in the body, a scar-like tissue encapsulates the sensor. The layer, even though it reduces the flow of blood or interstitial flood toward the sensor, works as a diffusion-limiting layer and greatly enhances the linearity of the sensor.

Measurement results reveal that the transponder chip functions properly providing that the amplitude of the received RF signal on the internal coil is higher than 2.6 V; the maximum distance between the external and the internal coils can be up to 4 cm; the circuit consumes a total current of about 110 μA. Table I summarizes the characteristics of the monitoring system.

VII. Discussion

When a device is to be implanted in the body, some considerations should be taken into account, such as biocompatibility of the device, implantation site, the effects of the body's immune system on the device, and packaging of the device. The packaging of our microsystem is explained in Section IV. In this section, we briefly discuss the other issues. We note that our sensor has not yet been used for in-vivo tests. We base our discussion on prior published implantation work from other researchers.

Our sensor is biocompatible since it is very similar to the conventional enzyme-based glucose biosensors which have proven to be biocompatible [41]. The only new material in the sensor is iridium oxide which is also biocompatible [42].

The implantation site is targeted to be just underneath the skin in the subcutaneous tissue where the implant will be in contact with interstitial fluid whose glucose content has good correlation with the blood glucose concentration [6].

When an electrochemical glucose sensor is implanted in the body, the body tries to reject the sensor as it does to other implants. Thus, during the first few days after implantation, the surrounding tissue continuously changes and causes the output signal of the sensor to drop or drift considerably. Therefore, the measurements are not very reliable during the first few days following implantation.

After a few days, the body encapsulates the implant in a thin scar-like tissue. Although the encapsulation results in a much lower amount of glucose reaching the sensing site, there is some evidence showing that it provides a more stable sensing environment. For example, in-vivo tests performed in the subcutaneous tissue of dogs have shown that the glucose sensors were inactive for the first few days, unstable for the next 7–14 days, and finally became relatively stable for the subsequent several weeks [9].

Another study reports a novel approach for improving the longevity, dynamic range, and stability of calibration of the subcutaneous sensors [13]. In this approach, an angiogenesis membrane and a bioprotective layer are added to the sensor membrane to first stimulate the development of capillaries around the sensor and, second, to reduce the body's immune system reaction. This approach shortens the early period of inconsistent monitoring and improves sensor lifetime. It proves the possibility of monitoring glucose in subcutaneous tissue for long periods of time (the mean lifetime of the sensors is reported as more than 100 days) [13].

The early period of inconsistent monitoring can be as early as six days or be delayed two or three months for reasons that are not yet clear [14]; but it is believed that miniaturization of the implant can minimize this period because the implant is then less sensitive to the patient's movements [14].

VIII. Conclusion

This paper has presented a miniaturization procedure for a wireless-implantable microsystem for continuous blood glucose monitoring. The microsystem receives inductive power from an external reader using a 13.56-MHz carrier, measures glucose concentration, and transmits the measured data back to the external reader using load-shift keying (LSK). The microsystem has a volume of 32 mm^3 and consists of an electrochemical glucose biosensor, a transponder chip, two surface-mount capacitors, and a hybrid coil inductor wound around the perimeter of the microsystem. The microsystem is designed to be implanted just underneath the skin. It is activated when the amplitude of the received RF signal at the internal coil is larger than 2.6 V.

A low-cost procedure for the microfabrication of the glucose sensor over a silicon substrate was presented along with the procedure for the hybrid integration of the microsystem. The system design as well as the circuit blocks of the transponder chip along with their measured results were described. The circuit realization of a simplified external reader has also been presented.

Acknowledgment

The authors would like to thank Prof. V. I. Birss and A. S. Jhas for their collaboration and helpful discussions that made this work possible. They would also like to thank Dr. C. Dalton and Dr. R. Potucek for their assistance with the enzyme-immobilization process and thank CMC Microsystems for the use of tools and fabrication technology.

References

[1] Diabetes Control and Complications Trial Research Group, "The effect of intensive treatment of diabetes on the development and progression of long-term complications in insulin-dependent diabetes mellitus," *New Engl. J. Med.*, vol. 329, no. 14, pp. 977–986, 1993.

[2] UK Prospective Diabetes Study (UKPDS) Group,, "Intensive blood-glucose control with sulphonylureas or insulin compared with conventional treatment and risk of complications in patients with type 2 diabetes (UKPDS 33)," *The Lancet*, vol. 352, no. 9131, pp. 837–853, Sep. 1998.

[3] Y. Ohkubo *et al.*, "Intensive insulin therapy prevents the progression of diabetic microvascular complications in Japanese patients with non-insulin dependent diabetes mellitus: A randomized prospective six year study," *Diabetes Res. Clin. Pract.*, vol. 28, no. 2, pp. 103–117, 1995.

[4] S. K. Garg, H. K. Hoff, and H. P. Chase, "The role of continuous glucose sensors in diabetes care," *Endocrinol. Metab. Clin. N. Am.*, vol. 33, pp. 163–173, 2004.

[5] D. C. Klonoff, "Continuous glucose monitoring: Roadmap for 21st century diabetes therapy," *Diabetes Care*, vol. 28, no. 5, pp. 1231–9, 2005.

[6] E. Kulcu, J. A. Tamada, G. Reach, R. O. Potts, and M. J. Lesho, "Physiological differences between interstitial glucose and blood glucose measured in human subjects," *Diabetes Care*, vol. 26, no. 8, pp. 2405–2409, 2003.

[7] B. D. McKean and D. A. Gough, "A telemetry instrumentation system for chronically implanted glucose and oxygen sensors," *IEEE Trans. Biomed. Eng.*, vol. 35, no. 7, pp. 526–532, Jul. 1988.

[8] M. C. Shults, R. K. Rhodes, S. J. Updike, B. J. Gilligan, and W. N. Reining, "A telemetry instrumentation system for monitoring multiple subcutaneously implanted glucose sensors," *IEEE Trans. Biomed. Eng.*, vol. 41, no. 10, pp. 937–942, Oct. 1994.

[9] B. J. Gilligan, M. C. Shults, R. K. Rhodes, and S. J. Updike, "Evaluation of a subcutaneous glucose sensor out to 3 months in a dog model," *Diabetes Care*, vol. 17, pp. 882–887, 1994.

[10] E. Wilkins, P. Atanosov, and B. A. Muggenburg, "Integrated implantable device for long-term glucose monitoring," *Biosensors Bioelectron.*, vol. 10, pp. 485–494, 1995.

[11] E. Wilkins and P. Atanosov, "Glucose monitoring: State of the art and future possibilities," *Med. Eng. Phys.*, vol. 18, no. 4, pp. 273–288, 1996.

[12] P. Atanasov, S. Yang, C. Salehi, A. L. Ghindilis, E. Wilkins, and D. Schade, "Implantation of a refillable glucose monitoring-telemetry device," *Biosensors Bioelectron.*, vol. 12, pp. 669–680, 1997.

[13] S. J. Updike, B. J. Gilligan, M. C. Shults, and R. K. Rhodes, "A subcutaneous glucose sensor with improved longevity, dynamic range, and stability of calibration," *Diabetes Care*, vol. 23, no. 2, pp. 208–214, 2000.

[14] B. J. Gilligan, M. C. Shults, R. K. Rhodes, P. G. Jacobs, J. H. Brauker, T. J. Pintar, and S. J. Updike, "Feasibility of continuous long-term glucose monitoring from a subcutaneous glucose sensor in humans," *Diabetes Technol Ther.*, vol. 6, no. 3, pp. 378–386, 2004.

[15] R. D. Beach, F. V. Kuster, and F. Moussy, "Towards a miniature implantable in-vivo telemetry monitoring system dynamically configurable as a potentiostat or galvanostat for two- and three-electrode biosensors," *IEEE Trans. Instrum. Meas.*, vol. 54, no. 1, pp. 61–72, Feb. 2005.
[16] A. P. F. Turner, I. Karube, and G. S. Wilson, *Biosensors: Fundamentals and Applications*. Oxford, U.K.: Oxford University Press, 1987.
[17] E. M. Abu Irhayem, "Fabrication and characterization of nanoparticulate and related iridium oxide-based glucose biosensors," Ph.D. dissertation, Univ. Calgary, Calgary, AB, Canada, 2004.
[18] A. S. Jhas, "Development of an electrode mediated glucose sensor using iridium oxide nanoparticles," M.Sc. dissertation, Univ. Calgary, Calgary, AB, Canada, 2007.
[19] T. Akin, K. Najafi, and R. M. Bradley, "A wireless implantable multichannel digital neural recording system for a micromachined sieve electrode," *IEEE J. Solid-State Circuits*, vol. 33, no. 1, pp. 109–118, Jan. 1998.
[20] D. A. Gough, K. Kreutz-Delgado, and T. M. Bremer, "Frequency characterization of blood glucose dynamics," *Ann. Biomed. Eng.*, vol. 31, no. 1, pp. 91–97, 2003.
[21] H. Banba *et al.*, "A CMOS bandgap reference circuit with sub-1-V operation," *IEEE J. Solid-State Circuits*, vol. 34, no. 5, pp. 670–674, May 1999.
[22] M. Ghovanloo and K. Najafi, "Fully integrated wideband high-current rectifiers for inductively powered devices," *IEEE J. Solid-State Circuits*, vol. 39, no. 11, pp. 1976–1984, Nov. 2004.
[23] P. Rakers, L. Connell, T. Collins, and D. Russell, "Secure contactless smartcard ASIC with DPA protection," *IEEE J. Solid-State Circuits*, vol. 36, no. 3, pp. 559–565, Mar. 2001.
[24] R. Reay, S. Kounaves, and G. Kovacs, "An integrated CMOS potentiostat for miniaturized electroanalytical instrumentation," in *Proc. IEEE Int. Solid-State Circuits Conf.*, 1994, pp. 162–163.
[25] R. Kakerow, H. Kappert, E. Spiegel, and Y. Manoli, "Low-power single-chip CMOS potentiostat," in *Proc. 8th Int. Conf. Solid-State Sensors Actuators*, 1995, pp. 142–145.
[26] Frey *et al.*, "Design of an integrated potentiostat circuit for CMOS bio sensor chips," in *Proc. IEEE Int. Symp. Circuits and Systems*, 2003, vol. 5, pp. 9–12.
[27] H. S. Narula and J. G. Harris, "VLSI potentiostat for amperometric measurements for electrolytic reactions," in *Proc. IEEE Int. Symp. Circuits and Systems*, 2004, vol. 1, pp. 457–460.
[28] S. Martin, F. Gebara, T. Strong, and R. Brown, "A low-voltage, chemical sensor interface for systems-on-chip: The fully differential potentiostat," in *Proc. IEEE Int. Symp. Circuits and Systems*, 2004, vol. 4, pp. 892–895.
[29] S. Martin, F. Gebara, B. J. Larivee, and R. Brown, "A CMOS-integrated microinstrument for trace detection of heavy metals," *IEEE J. Solid-State Circuits*, vol. 40, no. 12, pp. 2777–2786, Dec. 2005.
[30] R. Genov, M. Stanacevic, M. Naware, G. Cauwenberghs, and N. V. Thakor, "16-channel integrated potentiostat for distributed neurochemical sensing," *IEEE Trans. Circuits Syst. I*, vol. 53, no. 11, pp. 2371–2376, Nov. 2006.
[31] A. Gore, S. Chakrabartty, S. Pal, and E. C. Alocilja, "A multichannel femtoampere-sensitivity potentiostat array for biosensing applications," *IEEE Trans. Circuits Syst. I*, vol. 53, no. 11, pp. 2357–2363, Nov. 2006.
[32] M. Stanacevic, K. Murari, A. Rege, G. Cauwenberghs, and N. V. Thakor, "VLSI potentiostat array with oversampling gain modulation for wide-range neurotransmitter sensing," *IEEE Trans. Biomed. Circuits Syst.*, vol. 1, no. 1, pp. 63–72, Mar. 2007.
[33] M. M. Ahmadi and G. A. Jullien, "Current-mirror based potentiostats for three-electrode amperometric electrochemical sensors," *IEEE Trans. Circuits Syst. I*, 2009, to be published.
[34] M. M. Ahmadi and G. Jullien, "A low power CMOS potentiostat for bioimplantable applications," in *Proc. 5th Int. Workshop on System-on-Chip*, 2005, pp. 184–189.
[35] M. Lambrechts and W. Sansen, *Biosensors: Microelectrochemical Devices*. Washington, DC: IOP, 1992.
[36] A. J. Bard and L. R. Faulkner, *Electrochemical Methods: Fundamentals and Applications*, 2nd ed. New York: Wiley, 2001.
[37] R. Tummalo, *Fundamentals of Microsystem Packaging*. New York: McGraw-Hill, 2001.
[38] S. Zimmermann, D. Fienbork, B. Stoeber, A. W. Flounders, and D. Liepmann, "A microneedle-based glucose monitor: Fabricated on a wafer-level using in device enzyme immobilization," in *Proc. 12th Int. Conf. Solid-State Sensors, Actuators and Microsystems*, 2003, vol. 1, pp. 99–102.
[39] S. Bhattacharya, A. Datta, J. M. Berg, and S. Gangopadhyay, "Studies on surface wettability of poly (Dimethyl) siloxane (PDMS) and glass under oxygen-plasma treatment and correlation with bond strength," *J. Microelectromechan. Syst.*, vol. 14, pp. 590–597, 2005.
[40] M. M. Ahmadi, "A wireless implantable microsystem for continuous blood glucose monitoring," Ph.D. dissertation, Univ. Calgary, Calgary, AB, Canada, 2007.
[41] P. H. Kvist *et al.*, "Biocompatibility of an enzyme-based, electrochemical glucose sensor for short-term implantation in the subcutis," *Diabetes Technol Therapeut.*, vol. 8, no. 5, pp. 546–559, 2006.
[42] E. A. Irhayem, H. Elzanowska, A. S. Jhas, B. Skrzynecka, and V. Birss, "Glucose detection based on electrochemically formed Ir oxide films," *J. Electroanal. Chem.*, vol. 538-539, pp. 153–164, 2002.

Mohammad Mahdi Ahmadi (S'05–M'07) received the B.Sc. degree in biomedical engineering (Hons.) from Shahid Beheshti University, Tehran, Iran, in 2000, the M.Sc. degree in electronic engineering from Sharif University of Technology, Tehran, Iran, in 2002, and the Ph.D. degree in electrical engineering from the University of Calgary, Calgary, AB, Canada, in 2007.

His Ph.D. research was on developing a wireless-implantable microsystem for continuous blood glucose monitoring. Since 2007, he has been a member of the R&D Group at Sound Design Technologies Ltd., Burlington, ON, Canada. His research interests include analog, mixed-signal, and radio-frequency integrated-circuit (IC) design for biomedical and communication applications. He has also conducted research in the areas of BioMEMS and biomedical microsystems.

Dr. Ahmadi received awards at the 44th ISSCC/DAC and the third Analog Devices student circuit design contests. He was also the winner of the clearest message award at the 2006 Alberta Biomedical Engineering Conference, and is the recipient of the Robert B. Paugh Memorial Scholarship in Engineering in 2006.

Graham A. Jullien (M'71–SM'83–F'03–LF'08), recently retired as the iCORE Chair in Advanced Technology Information Processing Systems and the Director of the ATIPS Laboratories, Professor Emeritus in the Electrical and Computer Engineering Department, University of Calgary, Calgary, AB Canada. His long-term research interests are in the areas of integrated circuits (including SoC), very-large scale integrated signal processing, computer arithmetic, high-performance parallel architectures, and number-theoretic techniques. Since taking up his Chair position at the University of Calgary, he expanded his research interests to include security systems, nanoelectronic technologies, and biomedical systems. He was also instrumental, along with his colleagues, in developing an Integration Laboratory cluster to explore next-generation integrated microsystems. He has published many papers in refereed technical journals and conference proceedings.

Dr. Jullien is a Fellow of the Engineering Institute of Canada and, until recently, was a member of the Boards of Directors of DALSA Corp., CMC Microsystems, and Micronet R&D. He has served on the organizing and program committees of many international conferences and workshops over the past 35 years. He was the General Chair for the IEEE International Symposium on Computer Arithmetic in Montpellier in 2007, and was Guest Co-Editor of the IEEE Proceedings Special Issue on System-on-Chip: Integration and Packaging, in 2006.